A self-calibration scheme for two-dimensional free-form probing measurement under the assumption of rigid-body machine kinematic model

Abstract:

A major uncertainty contributor to the on-machine probing is linear axis kinematic errors. This paper proposes a novel self-calibration scheme to separate the workpiece geometry and machine tool kinematic errors from the probed profiles. Many self-calibration schemes have been well developed, but they are limited to either of the straightness, roundness, and two-dimensional (2D) grid point positions, since they require the probed points being in a closed set, as the workpiece is rotated or translated. This paper proposes its extension to a free-form 2D geometry. A key idea is on the assumption that the machine tool's positioning error is in accordance with the rigid-body kinematic model. It makes linear axis error motions, represented in a look-up table format, be in a closed set. Two experimental case studies are presented. The uncertainty assessment is essential to investigate the effectiveness of the proposed scheme for the given workpiece geometry.

Keywords: Self-calibration, On-machine measurement, Geometric error, Five-axis machine tool, metrology

1. Introduction

When measuring a geometric profile of a workpiece on a machine tool (MT), a touch-trigger probe is widely adopted in the industry due to its affordability [1]. The touch-trigger probe enables MT users to measure a machined workpiece on-site, similarly as coordinate measuring machines (CMMs) do, which leads to in-process assessment of product quality. Mutilba et al. [1] discusses key differences between a CMM and a MT; first, for on-machine measurement, the machining and measuring operations can be performed at the same machine. The machine geometric errors can affect both machining and measuring paths, and they may not be fully observable on the workpiece geometric errors measured by on-machine measurement. Secondly, non-controlled shop floor environment can be a major uncertainty source. Spindle rotation and the machining process can be a major internal heat source, which do not exist on CMMs.

Traceable on-machine measurement has been actively researched. A review can be found in [1]. It was intensively studied in a EURAMET project, Traceable in-process dimensional measurement, in 2013-2016 [2]. A technical report (TR) was lately proposed to the ISO (International Organization for Standardization) to standardize the evaluation of the measuring performance of "a MT as a CMM", which is currently under discussion in ISO TC39/SC2 [3]. Such activities clearly show recent industrial demands for traceable on-machine measurement.

As is well reviewed in [1], for traceable on-machine measurement, many researchers have studied its uncertainty assessment. In principle, the same uncertainty assessment methodologies for CMMs can be applied to MTs. Mutilba et al. [1] categorized the uncertainty assessment methodologies into a) the substitution method based on ISO 15530-3 [4], b) numerical simulation based on ISO 15530-4 [5], and c) the uncertainty budget method based on VDI 2617-11 [6]. For a) the substitution method, Klobucar and Acko [7] developed the ball bar artefact to check geometric errors of machining centres. Viprey et al. [8] developed a new thermo-invariant multi-feature bar artefact to indirectly identify MT geometric error. It was aimed to minimize the MT's downtime for calibration procedure. b) Regarding the quantitative evaluation of measurement uncertainty, the Virtual CMM concept is well-developed nowadays [9,10]. Virtual CMM simulates the error sources due to, for example, linear axes geometric errors, probe head, temperature, and software for a task-specific uncertainty estimation. In principle, the virtual CMM concept can be applied to the on-machine measurement on MTs, and such software is not commercially available now, but may be available in near future [3].

For traceable measurement by CMMs, the reverification or interim tests play an important role, as described in ISO 10360-2 [11] and -5 [12]. For MTs, numerous research works have been reported on the measurement of linear or rotary axis error motions, either directly [13] or indirectly [14][15]. In principle, they can be applied as reverification tests for MTs, or for numerical compensation of error motions to reduce the on-machine measurement uncertainty. For example, similarly as CMMs, the measurement of linear axis error motions by using an artefact of the pre-calibrated geometry has been commonly done [8,9,16,17]. The multilateration using a tracking interferometer [18][19] can evaluate all the error motions of all the linear axes. The ball bar tests can be for a quick interim check or for indirect measurement of error motions [20][21].

Some of such tests can take significant setup and measurement time. Furthermore, the reverification tests should be preferably done shortly before the measurement tasks to minimize the uncertainty contribution of environmental change. For MTs used for both machining and measurement, this can be considered as possibly significant machine downtime, and may not be acceptable from the viewpoint of machine operation cost. This is another potentially critical difference between CMMs and MTs.

This paper presents a different approach to cancel the influence of linear axis error motions on the uncertainty in the on-machine measurement on MTs – a self-calibration approach. Self-calibration schemes have been well established, but in the literature, they are limited only to the measurement of 1) the roundness of a nominally circular part, 2) the straightness of a nominally straight surface, and 3) the position of 2D grid points [22]. Figure 1(a) illustrates an example in [23][24] of the conventional self-calibration schemes for the roundness measurement of a nominally circular workpiece. The objective is to measure the workpiece's geometric error at the probed points, $G_{\text{normal, i}} \in \Re$ (i = 1, ... ,12). In this example, the points shown by red circules are probed with positioning by X- and Y-axes, and their positioning error in the direction normal to the surface is denoted by $E_{\text{normal, i, 1}} \in \Re$ (i = 1, ... ,12). The probed displacement at the i-th point is influenced by $G_{\text{normal, i}}$ and $E_{\text{normal, i, 1,}}$ which are both unknown. In this exmple, the objective of the self-calibration is to identify both $G_{\text{normal, i}}$ and $E_{\text{normal, i, 1}}$ for i = 1, ... ,12, and thus there are total 24 unknown variables to identify. As the workpiece is rotated (by 30° in Fig. 1a), nominally the same points are probed. The positioning error at each point can be seen approximately the same as the original setup, i,e. $E_{\text{normal,i,1}} \approx E_{\text{normal,i,2}}$ for any i. Thus, the number of unknown variables is still 24. This makes it possible to separately identify $G_{\text{normal, i}}$ and $E_{\text{normal, i, 1}}$. This illustrates a simplified concept of the conventional self-calibration schemes ("multi-step approach"). Many different self-calibration setups are available [22] but their essential idea is common.

This self-calibration can be applied only to a nominally circular workpiece. When a non-circular workpiece is rotated, as illustrated in Fig.1(b), the probed points can be completely different, which makes $E_{\text{normal, i, 1}} \neq E_{\text{normal, i, 2}}$ for any i. As a result, no matter how many times the workpiece is rotated, $G_{\text{normal, k}}$ and $E_{\text{normal, k, 1}}$ cannot be sepately identified. In Fig. 1(a), the unknown variables representing the machine's positioniong error, $E_{\text{normal, i, j}}$ (i=1, ... ,12), stay in a closed set, as the workpiece is rotated. This is one of the fundamental requirements for a self-calibration to be applied. Nominally straight surfaces, when moved parallel to the surface or is reversed, and 2D grid points, when moved to grid directions or rotated

by 90°, meet this requirement.

The self-calibration schemes for 1) circular and 2) straight surfaces and 3) 2D grids are well established. A commercial rotary encoder is available with multiple optical sensors based on the multi-probe self-calibration [25]. Huang [26] presented a self-calibration method to compensate for an ultra-precision air-bearing motion stage. Guenther et al. [27] applied a roundness self-calibration scheme to a circular ball artefact used for gear measurement. The straightness self-calibration schemes are effective particularly for ultra-precision machining applications (the reversal [28], multi-step and multi-probe methods [29][30]). The self-calibration schemes for 2D grids have been also popularly studied (the multi-probe method [31] and the multi-setup methods [32][33]).

The self-calibration techniques typically require performing multiple tests, and thus are time consuming. They can, however, separate the systematic deviations caused by the probing and the positioning system from the deviations of the measured object [27]. To reduce the on-machine measurement uncertainty, they can be more efficient, and practically feasible, than performing the verification tests frequently in a machine shop environment.

To significantly extend the applicability of self-calibration schemes, this paper proposes a novel self-calibration scheme to measure the geometry of an arbitrary 2D shape, based on the probing by two linear axes of unknown error motions. For an arbitrary geometry, a key idea is on the assumption that the machine's motion is in accordance with the rigid body kinematic model. In this kinematic model, the error motions of linear axes are described by a look-up table with its nominal position as an input. The values in the error motion look-up tables are unknown variables to be identified, and they are in a closed set, as the object rotates, and more points are probed. This makes it possible to apply a self-calibration scheme. As reviewed in [14][15], numerous researchers have presented measurement or compensation schemes of linear axis volumetric errors based on this rigid-body assumption. The validity of the rigid-body kinematic model has been well verified on many typical machine tools. An innovative contribution of this work is its application to the self-calibration for the measurement of workpiece geometry. As illustrated in Fig. 1, this application enables the self-calibration for an arbitrary 2D geometry, which is not possible by conventional self-calibration schemes.

The algorithm proposed in this paper is extended from the one presented in our previous works [23][24]. An essential difference is, firstly, that Refs. [23][24] presented a self-calibration scheme for a nominally circular workpiece, which can be seen as a variant of the conventional self-calibration schemes. For the first time, this paper proposes an extension of the self-calibration schemes to an arbitrary 2D geometry. Secondly, a primal objective of the algorithms in Refs. [23][24] is to separately quantify the kinematic errors of rotary and linear axes. The geometric error of the nominally circular workpiece is identified as a byproduct. A primal objective of the algorithm presented in this paper is to identify the workpiece geometry error under the existence of linear axis error motions.

The uncertainty in the workpiece geometry estimated by the proposed scheme can heavily depend on its nominal geometry. Thus, the uncertainty assessment, presented in Section 6, is essential. In Section 5, two experimental case studies are presented to demonstrate the effectiveness of the present scheme.

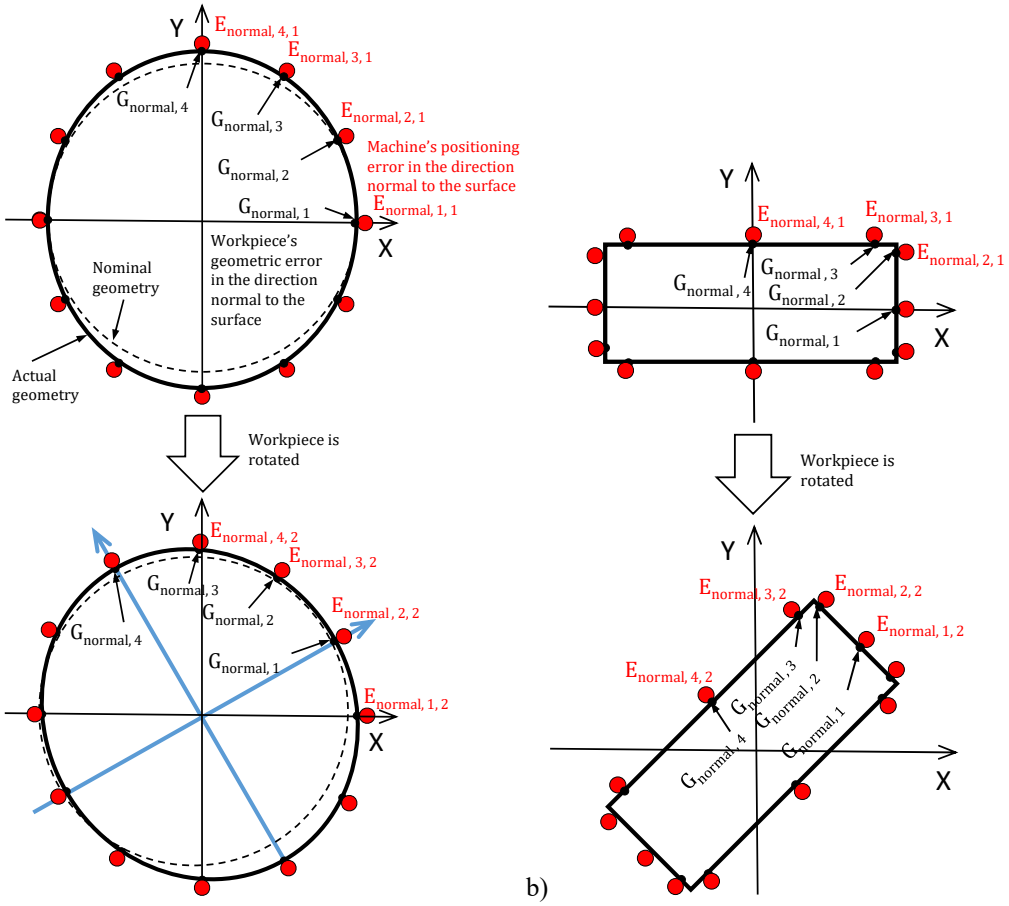

Figure 1 Concept of the conventional self-calibration and its limitation. a) An example self-calibration setup to measure the roundness of a nominally circular workpiece by probing the points shown by red circules. The objective is to measure the workpiece's geometric error at the probed points, $G_{\text{normal, i}}$ (i =1, ... ,12). The machine's positioing error in the direction normal to the surface, $E_{\text{normal, i, 1}}$ is also unknown. When the workpiece is rotated and the same points are probed, $G_{\text{normal, i}}$ and $E_{\text{normal, i, 1}}$ can be sepearatedly identified, since $E_{\text{normal, i, 1}} \approx E_{\text{normal, i, 2}}$ for any i. b) When a non-circular workpiece is rotated, the probed points can be completely different, which makes $E_{\text{normal, i, 1}} \neq E_{\text{normal, i, 2}}$ for any i. Thus, $G_{\text{normal, k}}$ and $E_{\text{normal, k, 1}}$ cannot be sepately identified.

2. Proposed measurement procedure and objective

2.1 Proposed measurement procedure

The objective is to measure the 2D geometry of an object workpiece by using a touch-trigger probe. Figure 2(a) shows an example. Red dots represent the target points to be probed. The objective is to measure the intersection of the workpiece contour with a line normal to it at every nominal probed point. The nominal position of the i-th probed point is denoted by ${}^{w}p_i^* = ({}^{w}x_i^*, {}^{w}y_i^*)$ $(i = 1,2,\dots,N_w$, where N_w is the number of measurement points). The left-side superscript, '^{w} ', represents a vector in the workpiece coordinate system (WCS). The WCS, denoted by ${}^{w}X$-${}^{w}Y$ in Figs. 2(a) and 2(b), is a CS that rotates by the rotary table (C-axis), with its origin at the actual position of the C-axis centerline. Throughout this paper, a symbol with the superscripted asterisk (*) represents the nominal value.

A touch-trigger probe, widely adopted with numerically controlled MTs, gives a binary signal as a result of contact with a surface being measured (called a "switching probe" in ISO 230-10 [34]). Figure 3 illustrates the measuring principle of a touch-trigger probe. When a machine tool controller receives this signal, the positions of the linear axes are measured by length measuring sensors for the axes, such as a linear encoder, which give the stylus sphere center position in the moment of the contact. When the machine tool has geometric errors, the position measured by the encoders may not give the exact position of the stylus sphere, as discussed in many past works reviewed in Section 1. Thus, the machine tool geometric errors can be major uncertainty contributors in the touch-trigger measurement. To reduce their influence, this paper proposes the following measurement procedure.

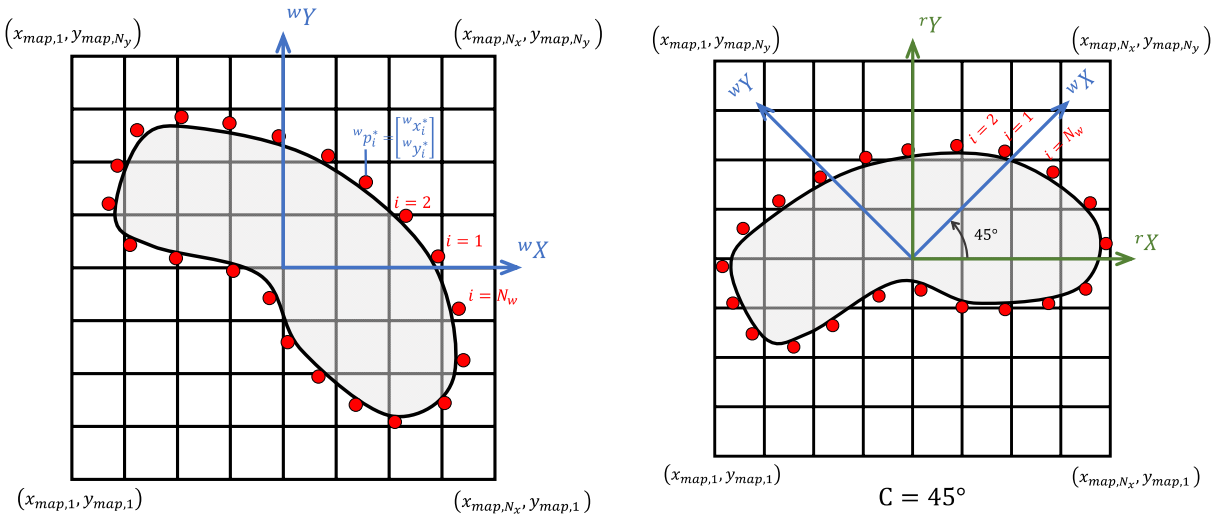

Figure 2 Probed points in the proposed measurement scheme (example setups with C=0° and C=45°). (a) at C=0°, (b) at C=45°.

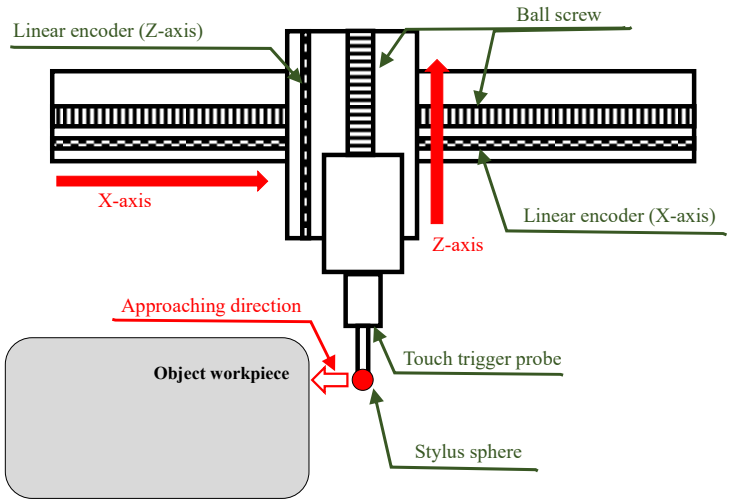

Figure 3 Configuration of a touch-trigger measurement system

The workpiece must be mounted on a rotary table (C-axis). This paper targets a vertical five-axis machine tool of the configuration shown in Fig. 4. The proposed scheme can be applied to any machines that have two orthogonal linear axes, and a rotary axis to rotate a workpiece around the centerline perpendicular to the measured plane. As illustrated in Fig. 2, the proposed method measures the same points (the same in the WCS) at different C angles. The C angles should be chosen based on the assessment of the uncertainty in the estimated object geometry (see Section 6). Figure 2 merely shows example setups with C=0° and C=45°.

Suppose that the C-axis is indexed at j-th angle, C_j $(j = 1,2,\dots,N_c$, where N_c is the number of C-axis angular positions). Complying with the sign convention of machine tool axes, C_j is defined positive clockwise. The i-th nominal point on the object workpiece in the WCS, $^wp_i^* \in \mathbb{R}^2$, can be converted to $^rp_{i,j}^* \in \mathbb{R}^2$ in the machine CS (MCS), which is given by:

$$^rp_{i,j}^* = R(-C_j) \cdot {}^wp_i^* \tag{1}$$

$$R(-C_j) = \begin{bmatrix} \cos(-C_j) & -\sin(-C_j) \\ \sin(-C_j) & \cos(-C_j) \end{bmatrix} \tag{2}$$

The MCS is the fixed CS with its origin at the nominal position of the C-axis centerline. The left-hand side superscript, '^{r}', represents a vector in the MCS. For this point, suppose that the actual probed point (contact point) is given in the MCS by $^r\tilde{p}_{i,j} \in \mathbb{R}^2$. Throughout this paper, a symbol with tilde, '$\tilde{}$', represents the measured value. A touch-trigger probe is sensitive only to the target point's position in the direction normal to the surface. Suppose that the unit vector normal to

the workpiece surface at this point is given in the MCS by ${}^{r}n_{i,j}^{*} \in \mathbb{R}^2$. Then, a probe can measure the projection of the 2D displacement to the direction normal to the surface, namely:

$$\Delta\tilde{q}_{i,j} = {}^{r}n_{i,j}^{*} \cdot \left({}^{r}\tilde{p}_{i,j} - {}^{r}p_{i,j}^{*} \right) \tag{3}$$

This is measured for all the points ($i = 1,2, \dots, N_w$) at all the C angles ($j = 1,2, \dots, N_c$). Note that $\Delta\tilde{q}_{i,j}$ is a scalar and thus irrelevant to the CS.

The distance between the point of first material contact of the stylus sphere with the surface being measured and the point where the probe signal is generated is called the pre-travel [34]. The pre-travel typically varies with the approaching direction. This paper assumes that the pre-travel variation is properly evaluated, as described in [34], and is compensated for. This paper does not consider the uncertainty attributable to the probe itself. This paper only considers the measurement error caused by the kinematic errors of X-, Y- and C-axis.

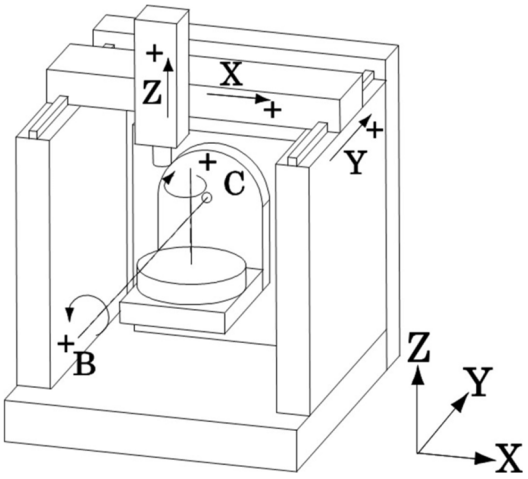

Figure 4 Configuration of the machine tool

2.2 Error variables to be identified

The touch-trigger probe is positioned by two linear axes, X and Y axes. Thus, its probed position is influenced by not only the geometry of the test piece, but also the error motions of X and Y axes. The proposed self-calibration scheme requires rotating the test piece by a rotary table (C-axis), and thus the C-axis error motions can also influence. Therefore, the objective of the proposed scheme is to identify all the error variables shown in Table 1.

a. Workpiece geometric errors

$G_{\text{normal}}({}^{w}p_i^{*})$ in Table 1 represents the geometric error of the workpiece from the nominal position, ${}^{w}p_i^{*}$, in the direction normal to the probed surface. Figure 5 illustrates its definition. The most important objective of the proposed algorithm is to identify it for all the points ($i = 1,2, \dots, N_w$).

b. Error motions of X- and Y-axes

Many past works on machine tool volumetric error measurement and compensation, reviewed in Section 1, assume the rigid-body kinematic model to relate error motions of each axis to the tool center point position. This paper adopts the same model. Gao et al. [15] presented a comprehensive review on machine tool calibration, and its Section 4.1 is devoted to the modeling theory of this quasi-static rigid-body kinematic model. For the derivation of the model below, see [15] and its references.

When the stylus sphere is positioned at the command position, $(x_{map,k}, y_{map,l})$, the positioning error in the X- and Y-directions are respectively modelled by:

$$E_{X,\text{total}}(x_{map,k}, y_{map,l}) = E_{XX}(x_{map,k}) + E_{XY}(y_{map,l}) - y_{map,l}E_{C(0X)Y} \tag{4}$$

$$E_{Y,\text{total}}(x_{map,k}, y_{map,l}) = E_{YX}(x_{map,k}) + E_{YY}(y_{map,l}) + x_{map,k}E_{CY}(y_{map,l}) \tag{5}$$

E symbols contained in the right-hand side of Eqs. (4) and (5), e.g. $E_{XX}(x_{map,k})$, represent the error motions of X- or Y-axes, and are described in Table 1. These notations comply with ISO 230-1 [35]. Each error motion of X- (or Y-) axis varies with the command X (or Y) position. In the proposed scheme, the X-axis error motions are defined at a discrete set of the X position, $x_{map,k}$ ($k = 1,2, \dots, N_x$). In other words, they are represented in a look-up table with total N_x parameters. Similarly, the error motions of Y-axis are defined at $y_{map,l}$ with $l = 1,2, \dots, N_y$. In other words, the error motions of X- and Y-axes are defined on 2D grid points, $(x_{map,k}, y_{map,l})$. Figure 6 illustrates linear axis geometric errors, defined on the grid points. When both X- and Y-axes are positioned, the kinematic model, Eqs. (4) and (5), formulates the X and Y positioning errors at every grid point, $(x_{map,k}, y_{map,l})$, as illustrated in Fig. 6.

The proposed scheme identifies the X- and Y-axis error motions, from $E_{XX}(x_{map,k})$ to $E_{CY}(y_{map,l})$ in Table 1, at every $k = 1,2,\dots,N_x$ and $l = 1,2,\dots,N_y$, as well as the squareness error of Y- to X-axis, $E_{C(0X)Y}$.

c. Error motions of C-axis

Similarly, when C-axis is indexed at C_j, the displacement of C-axis in the X- and Y-directions are represented by $E_{XC,\text{total}}(C_j)$ and $E_{YC,\text{total}}(C_j)$, and its angular positioning error motion is represented by $E_{CC}(C_j)$, defined at a discrete set of C_j $(j = 1,2,\dots,N_c)$. $E_{XC,\text{total}}(C_j)$ and $E_{YC,\text{total}}(C_j)$ contains both the radial error motion of C-axis and the position error of C-axis average line [36], as described in Table 1.

The proposed scheme also identifies the C-axis error motions, from $E_{XC,\text{total}}(C_j)$ to $E_{CC}(C_j)$ in Table 1, at every $j = 1,2,\dots,N_c$. The total number of the error variables contained in Table 1 is $N_w + 2N_x + 3N_y + 1 + 3N_c$. The objective of the algorithm is to identify all of them.

Table 1 Error variables to be identified by the proposed scheme

Variable	Description
$G_{\text{normal}}({}^{w}p_i^*)$	Geometric error of the workpiece from the nominal position $({}^{w}x_i^*, {}^{w}y_i^*)$ in the direction normal to the probed surface.
$E_{XX}(x_{map,k})$	Linear positioning error of X-axis.
$E_{YX}(x_{map,k})$	Straightness error of X-axis in the Y-direction.
$E_{XY}(y_{map,l})$	Straightness error of Y-axis in the X-direction.
$E_{YY}(y_{map,l})$	Linear positioning error of Y-axis.
$E_{CY}(y_{map,l})$	Yaw of Y-axis.
$E_{C(0X)Y}$	Squareness error between X- and Y-axis.
$E_{XC,\text{total}}(C_j)$	Displacement of C-axis in the X-direction when C-axis is indexed at C_j. It is given by the superposition of the X position error of the C-axis average line, E_{X0C},and the radial error motion, E_{XC}, in the X-direction as a function of the rotation angle C_j: $E_{XC,\text{total}}(C_j) = E_{X0C} + E_{XC}(C_j)$.
$E_{YC,\text{total}}(C_j)$	Displacement of C-axis in the Y-direction when C-axis is indexed at C_j. It is given by the superposition of the Y position error of the C-axis average line, E_{Y0C},and the radial error motion, E_{YC}, in the X-direction as a function of the rotation angle C_j: $E_{YC,\text{total}}(C_j) = E_{Y0C} + E_{YC}(C_j)$.
$E_{CC}(C_j)$	Angular positioning deviation of C-axis when C-axis is indexed at C_j.

List of subscripts

i: index number of the probed points ($i = 1,2,\dots,N_w$), see Fig. 1.
j: index number of command C-axis angular positions ($j = 1,2,\dots,N_c$).
k, l: index number of grid points in X and Y directions, respectively ($k = 1,2,\dots,N_x, l = 1,2,\dots,N_y$), see Fig. 5.

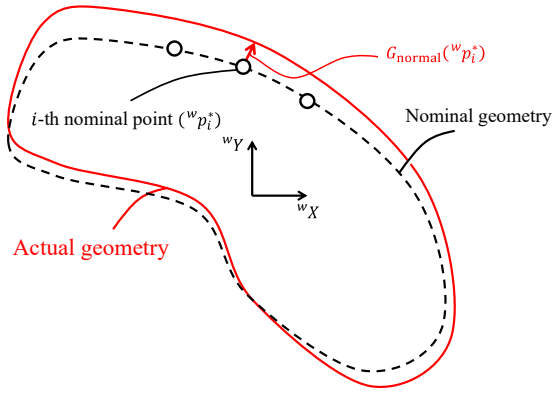

Figure 5 Definition of geometric error of the workpiece, $\boldsymbol{G_{\text{normal}}({}^{w}p_i^*)}$

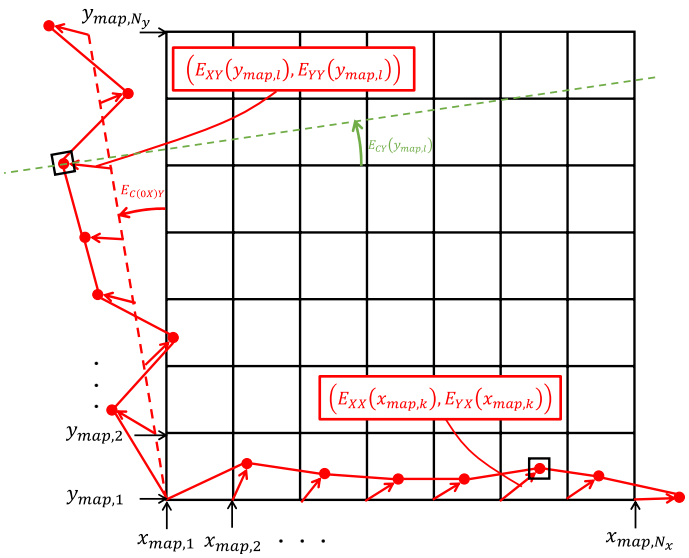

Figure 6 Definition of X- and Y-axis error motions, $\boldsymbol{E_{XX}(x_{map,k})}$, $\boldsymbol{E_{YX}(x_{map,k})}$, $\boldsymbol{E_{XY}(y_{map,l})}$, $\boldsymbol{E_{YY}(y_{map,l})}$, $\boldsymbol{E_{CY}(y_{map,l})}$

3. Proposed self-calibration algorithm

3.1 Concept of the self-calibration scheme

When a workpiece of free-form geometry is indexed at N_c angles, as shown in Fig. 2, and N_w points are probed at every C angle, the total number of probed points is N_wN_c. If the (X, Y) positioning error of the probe is completely independent and unknown at every probed point, the number of unknown parameters is $2N_wN_c$, since the probed points are generally different in the MCS at every C angle. Since the number of unknown parameters is always larger than the number of measurements, it is clearly impossible to separately identify the probe positioning errors, regardless of N_c. In other words, in this scheme, probed points are not in a closed set, which makes it impossible to apply the conventional self-calibration. This was illustrated in Fig. 1b.

The proposed scheme assumes the kinematic model in Eqs. (4) and (5), where error motions are represented only at the prescribed discrete set of command positions, as shown in Table 1. In other words, in the proposed scheme, the variables representing the positioning error by X- and Y-axes, namely $E_{XX}(x_{map,k})$, $E_{YX}(x_{map,k})$, $E_{XY}(y_{map,l})$, $E_{YY}(y_{map,l})$, $E_{CY}(y_{map,l})$, and $E_{C(0X)Y}$ $(k = 1,2,\dots,N_x, l = 1,2,\dots,N_y)$ in Table 1, are in a closed set. The number of unknown parameters representing the probe positioning errors becomes $2N_x + 3N_y + 1$. Then, by increasing N_c, the number of the probed points eventually exceeds the number of the parameters to be identified. This is a fundamental idea behind the algorithm proposed in the following subsection.

The total number of variables to be identified in Table 1 is $N_w + 2N_x + 3N_y + 1 + 3N_c$, while the number of the probed points is N_w for each angle C angle. Therefore, the minimum requirement for the estimation of the error parameters is:

$$N_w + 2N_x + 3N_y + 1 + 3N_c < N_wN_c \tag{6}$$

The number of C-axis angular positions, N_c, must meet this condition.

3.2 Formulation of the probed displacement

The measured errors by the probe, $\Delta\tilde{q}_{i,j}$, given in Eq. (3), are influenced by three error sources, a) the geometric error of the workpiece, $G_{\text{normal}}({}^{w}p_i^*)$, b) the positioning error of linear axes, $\left[E_{X,\text{total}}({}^{r}x_{i,j}^*, {}^{r}y_{i,j}^*), E_{Y,\text{total}}({}^{r}x_{i,j}^*, {}^{r}y_{i,j}^*)\right]^T$, c) the displacement of C-axis in X and Y directions, $\left[E_{XC,\text{total}}(C_j), E_{YC,\text{total}}(C_j)\right]^T$, and the angular positioning deviation of C-axis, $E_{CC}(C_j)$. Each influence is formulated as follows:

a. Influence of workpiece geometric error
As is described in Section 2.2 a, the workpiece's geometric error, $G_{\text{normal}}({}^{w}p_i^*)$, is defined in the WCS. Regardless of the C-axis angular position, C_j, its influence on the probed displacement is given by:

$$\Delta\hat{q}_{i,j,1} = G_{\text{normal}}({}^{w}p_i^*) \tag{7}$$

This formulation is depicted in Fig. 7 (a).

b. Influence of linear axis error motions

As illustrated in Fig. 6, the linear axis error motions are defined only on grid points, $(x_{map,k}, y_{map,l})$. When the C-axis is indexed at C_j, the nominal probed point in the MCS, ${}^{r}p^{*}_{i,j} = ({}^{r}x^{*}_{i,j}, {}^{r}y^{*}_{i,j})$, is given by Eq. (1). The positioning error at this point is given by linearly interpolating Eqs. (4) and (5). The detailed formulation will follow.

Find $1 \le k \le N_x - 1$ and $1 \le l \le N_y - 1$ such that $x_{map,k} \le {}^{r}x^{*}_{i,j} \le x_{map,(k+1)}$ and $y_{map,l} \le {}^{r}y^{*}_{i,j} \le y_{map,(l+1)}$. Define:

$$\zeta({}^{r}x^{*}_{i,j}) = \frac{{}^{r}x^{*}_{i,j} - x_{map,k}}{x_{map,(k+1)} - x_{map,k}} \tag{8}$$

$$\eta({}^{r}y^{*}_{i,j}) = \frac{{}^{r}y^{*}_{i,j} - y_{map,l}}{y_{map,(l+1)} - y_{map,l}} \tag{9}$$

Then, the positioning error at ${}^{r}p^{*}_{i,j}$ is given by linearly interpolating Eqs. (4) and (5) as:

$$\begin{aligned} E_{X,\text{total}}({}^{r}x^{*}_{i,j}, {}^{r}y^{*}_{i,j}) &= \left(1 - \zeta({}^{r}x^{*}_{i,j})\right) E_{XX}(x_{map,k}) + \left(1 - \eta({}^{r}y^{*}_{i,j})\right) E_{XY}(y_{map,l}) \\ &+ \zeta({}^{r}x^{*}_{i,j}) E_{XX}(x_{map,(k+1)}) + \eta({}^{r}y^{*}_{i,j}) E_{XY}(y_{map,(l+1)}) - {}^{r}y^{*}_{i,j} E_{C(0X)Y} \end{aligned} \tag{10}$$

$$\begin{aligned} E_{Y,\text{total}}({}^{r}x^{*}_{i,j}, {}^{r}y^{*}_{i,j}) &= \left(1 - \zeta({}^{r}x^{*}_{i,j})\right) E_{YX}(x_{map,k}) + \left(1 - \eta({}^{r}y^{*}_{i,j})\right) E_{YY}(y_{map,l}) + \left(1 - \eta({}^{r}y^{*}_{i,j})\right) {}^{r}x^{*}_{i,j} E_{CY}(y_{map,l}) \\ &+ \zeta({}^{r}x^{*}_{i,j}) E_{YX}(x_{map,(k+1)}) + \eta({}^{r}y^{*}_{i,j}) E_{YY}(y_{map,(l+1)}) + \eta({}^{r}y^{*}_{i,j}) {}^{r}x^{*}_{i,j} E_{CY}(y_{map,(l+1)}) \end{aligned} \tag{11}$$

Its projection onto the direction normal to the target surface, given by ${}^{r}n^{*}_{i,j}$ in Eq. (3), gives the influence on the probed displacement by:

$$\Delta\hat{q}_{i,j,2} = -\,{}^{r}n^{*}_{i,j} \cdot \begin{bmatrix} E_{X,\text{total}}({}^{r}x^{*}_{i,j}, {}^{r}y^{*}_{i,j}) \\ E_{Y,\text{total}}({}^{r}x^{*}_{i,j}, {}^{r}y^{*}_{i,j}) \end{bmatrix} \tag{12}$$

This formulation is depicted in Fig. 7 (b).

c. Influence of C-axis error motions

Similarly, when C-axis is indexed at the angular position, C_j, the displacement of C-axis, $[E_{XC,\text{total}}(C_j), E_{YC,\text{total}}(C_j)]^T$, and the angular positioning deviation of C-axis, $E_{CC}(C_j)$, influence the probed displacement, $\Delta\tilde{q}_{i,j}$, by their projection in the direction normal to the target surface. Their influence is formulated by:

$$\Delta\hat{q}_{i,j,3} = {}^{r}n^{*}_{i,j} \cdot \begin{bmatrix} E_{XC,\text{total}}(C_j) \\ E_{YC,\text{total}}(C_j) \end{bmatrix} + R(90°) \cdot {}^{r}p^{*}_{i,j} \cdot {}^{r}n^{*}_{i,j} \cdot E_{CC}(C_j) \tag{13}$$

This formulation is depicted in Fig. 7 (c).

d. Overall formulation of the probed displacement

Combining a, b and c, the influence of the error sources in Table 1 on the probed displacements can be formulated as follows:

$$\Delta\hat{q}_{i,j} = \Delta\hat{q}_{i,j,1} + \Delta\hat{q}_{i,j,2} + \Delta\hat{q}_{i,j,3} \tag{14}$$

a)

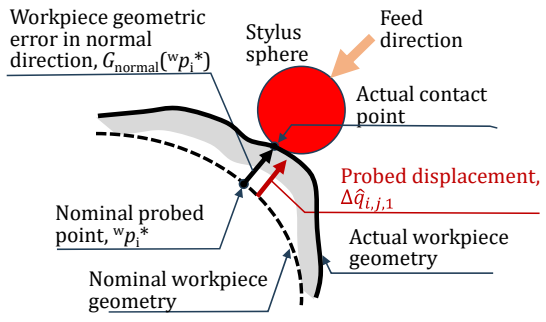

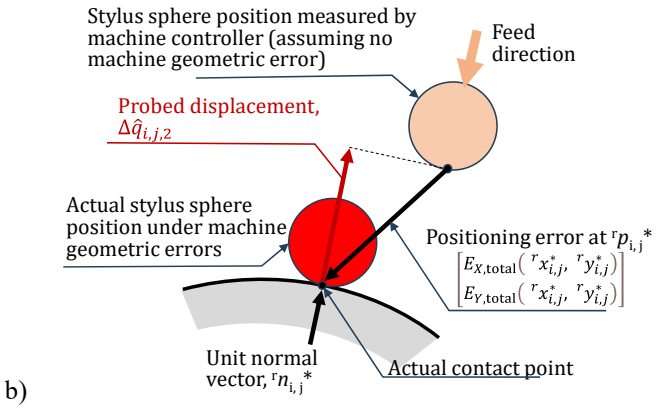

b)

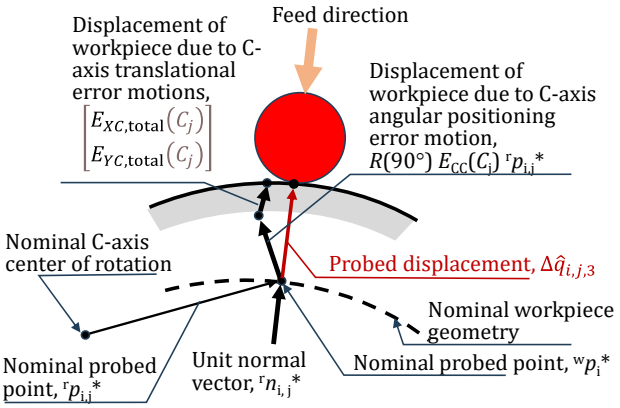

c)

Figure 7 Influence of a) the workpiece geometric error $G_{\text{normal}}({}^{w}p_{i}^{*})$, b) the machine tool positioning error, $[E_{X,\text{total}}({}^{r}x^{*}_{i,j},\ {}^{r}y^{*}_{i,j}),\ E_{Y,\text{total}}({}^{r}x^{*}_{i,j},\ {}^{r}y^{*}_{i,j})]^{\text{T}}$, and c) the C-axis angular positioning error motion, $E_{CC}(C_j)$, and C-axis translational error motion, $[E_{XC,\text{total}}(C_j), E_{YC,\text{total}}(C_j)]^{T}$, on the probed displacement in the direction normal to the target surface.

3.3 Self-calibration algorithm to identify error sources

When C-axis is indexed at C_j $(j = 1,2,\dots,N_c)$, N_w points are probed at ${}^{r}p^{*}_{i,j}$ $(i = 1,2,\dots,N_w)$. Combining all the $N_w N_c$ points, Eq. (14) can be equivalently converted to a matrix form:

$$\begin{bmatrix} \Delta\hat{q}_{1,1} \\ \vdots \\ \Delta\hat{q}_{N_w,N_c} \end{bmatrix} = \boldsymbol{A}_{\mathbf{normal}} \begin{bmatrix} \vdots \\ E_{XX}(x_{map,k}) \\ E_{YX}(x_{map,k}) \\ E_{XY}(y_{map,l}) \\ E_{YY}(y_{map,l}) \\ E_{CY}(y_{map,l}) \\ E_{XX}(x_{map,(k+1)}) \\ E_{YX}(x_{map,(k+1)}) \\ E_{XY}(y_{map,(l+1)}) \\ E_{YY}(y_{map,(l+1)}) \\ E_{CY}(y_{map,(l+1)}) \\ \vdots \\ E_{C(0X)Y} \\ G_{\text{normal}}({}^{w}p_1^*) \\ \vdots \\ G_{\text{normal}}({}^{w}p_{N_w}^*) \\ E_{XC,\text{total}}(C_1) \\ E_{YC,\text{total}}(C_1) \\ E_{CC}(C_1) \\ \vdots \\ E_{XC,\text{total}}(C_{N_c}) \\ E_{YC,\text{total}}(C_{N_c}) \\ E_{CC}(C_{N_c}) \end{bmatrix} \tag{15}$$

where $\boldsymbol{A}_{\mathbf{normal}}$ matrix has the size of $N_w N_c \times (N_w + 2N_x + 3N_y + 1 + 3N_c)$. To eliminate the rank deficiency in $\boldsymbol{A}_{\mathbf{normal}}$, firstly, the following boundary conditions should be imposed to define the origin of MCS:

$$\begin{cases} E_{XX}(0) = 0 \\ E_{YX}(0) = 0 \\ E_{XY}(0) = 0 \\ E_{YY}(0) = 0 \\ E_{CY}(0) = 0 \\ E_{XC,\text{total}}(C_{j=1}) = 0 \\ E_{YC,\text{total}}(C_{j=1}) = 0 \\ E_{CC}(C_{j=1}) = 0 \end{cases} \tag{16}$$

Additionally, the following three boundary conditions should be imposed to define the X- and Y-direction of MCS and the "absolute" length of X-axis:

$$\begin{cases} E_{YX}(x_{map,N_x}) = 0 \\ E_{XY}\left(y_{map,N_y}\right) = 0 \\ E_{XX}(x_{map,N_x}) = \Delta L \end{cases} \tag{17}$$

where ΔL is the X-axis linear positioning error at (x_{map,N_x}, y_1), which must be directly measured. Analogous to the self-calibration for a nominally circular workpiece presented in [23], the present self-calibration method cannot estimate the "absolute" distance. This can be seen an inherent limitation common in many self-calibration schemes [22]. The linear positioning error of the X-axis, ΔL in Eq. (17), must be directly measured between two points, X=0 and x_{map,N_x}. It can be measured by, for example, probing an artefact of the pre-calibrated length. Note that it is not needed to measure other points in the X-direction, $E_{XX}(x_{map,2})$ to $E_{XX}(x_{map,N_x-1})$, and to measure the Y-axis, $E_{YY}(y_{map,1})$ to $E_{YY}(y_{map,N_y})$; they can be estimated by the proposed algorithm.

With eleven boundary conditions (Eqs. (16) and (17)) imposed, $\boldsymbol{A}_{\mathbf{normal}}$ becomes full rank. Then, when the workpiece's displacement, $\Delta\tilde{q}_{i,j}$ given by Eq. (3), is measured by the probe at all i-th points and the j-th C-axis angular positions, the vector containing error parameters in the right-hand side of Eq. (15), denoted by $\Theta \in \mathbb{R}^{(N_w+2N_x+3N_y+1+3N_c)\times 1}$, can be identified by solving the following minimization problem by using the least square method:

$$\min_{\Theta} \sum_{j=1}^{N_c} \sum_{i=1}^{N_w} \left(\Delta\tilde{q}_{i,j} - \Delta\hat{q}_{i,j} \right)^2 \tag{18}$$

4. Case study #1: Experimental validation of the proposed scheme with a cross-shaped pocket

4.1 Test objective

The objective of the experiment is to investigate the effectiveness of the proposed self-calibration scheme in improving the measurement accuracy of the workpiece geometric error under unknown linear axis error motions. The workpiece's geometric profile, estimated by the proposed scheme, is compared to the CMM measurement. The 2D positioning errors of X- and Y-axes, estimated by the proposed scheme, is compared to their direct measurement by using a 2D digital scale.

Additionally, as will be discussed in Section 6, the estimation uncertainty of the proposed scheme can heavily depend on the workpiece nominal geometry. For the workpiece geometry in the present experiment (Fig. 8), Section 6 will assess that the uncertainty in the estimated workpiece can be reduced by adding extra probed points on precision spheres attached to the workpiece. This will be experimentally validated. This is another objective of the present case study.

4.2 Experimental procedure

A cross-shaped pocket of the geometry shown in Fig. 8 was fixed on a rotary table (C-axis) of a vertical five-axis machining center, NMV 3000 DCG by DMG Mori. Co., Ltd. of the configuration shown in Fig. 4. The machined pocket has 36 mm in width and 10 mm in depth. The surface roughness of machined part was sufficiently small not to influence the probing. The workpiece material is a carbon steel, JIS S45C. The center of the workpiece was roughly aligned to the C-axis centerline. The workpiece was machined by the same machining center. In conventional probing operations, this can cause a measurement error. When machining and probing paths are similar, the machine tool error motions copied onto the workpiece geometric errors in the machining may not be observable by the touch-trigger probing. By applying the proposed self-calibration scheme, the workpiece's geometry can be measured with canceling the influence of machine tool error motions, even when the workpiece was machined by the same machine tool.

Renishaw OMP400 touch-trigger probe was installed to the spindle (major specifications in the manufacturer's catalog: Unidirectional repeatability (2σ): 0.35 μm for stylus length 100 mm, 3D pre-travel variation in X, Y, Z: ±1.75 μm for stylus length 100 mm). The diameter of the stylus sphere was 6 mm. According to the suggestion by the uncertainty analysis in Section 6, to add extra probed points to reduce the uncertainty, two precision spheres (diameter: 25.4 mm, sphericity: 1 μm) were attached on the workpiece by a neodymium magnet. Their center positions in the MCS were measured by using the probe.

The nominal probed targets (total $N_w = 92$ points), ${}^{w}p_i^*$, are shown in Fig. 8(b). The points on the cross-shaped pocket were measured at the same Z position (3 mm lower than the workpiece top surface). The points on the spheres are on their equator. All the points were measured at:

$$C = 0°, 75°, 130°, 210° \tag{19}$$

These C angles were decided based on the uncertainty analysis discussed in Section 6. The measurement cycle at each C angle took approximately 15 minutes. The grid, where X- and Y-axis error motions are defined (see Fig. 6), was set with $x_{map,k} = -110, -88, -66, \dots, +110$ mm and $y_{map,l} = -110, -88, -66, \dots, +110$ mm (10×10 grid).

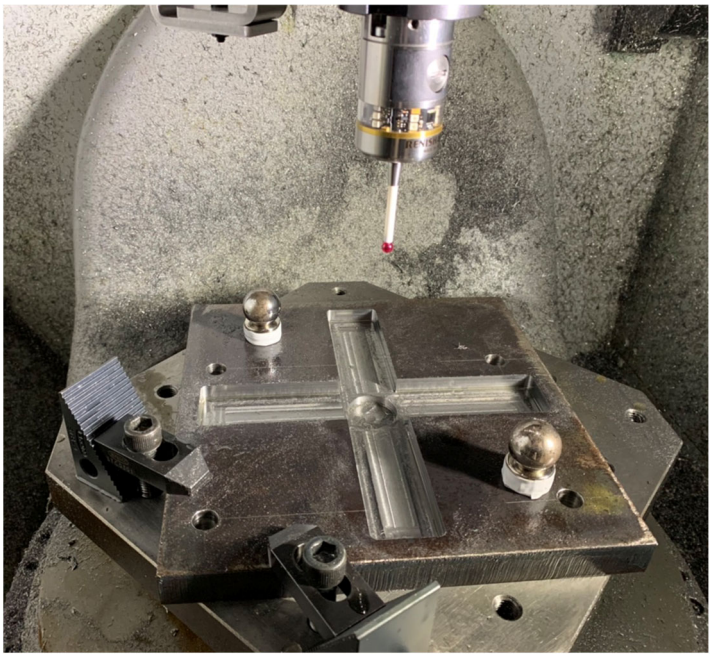

(a)

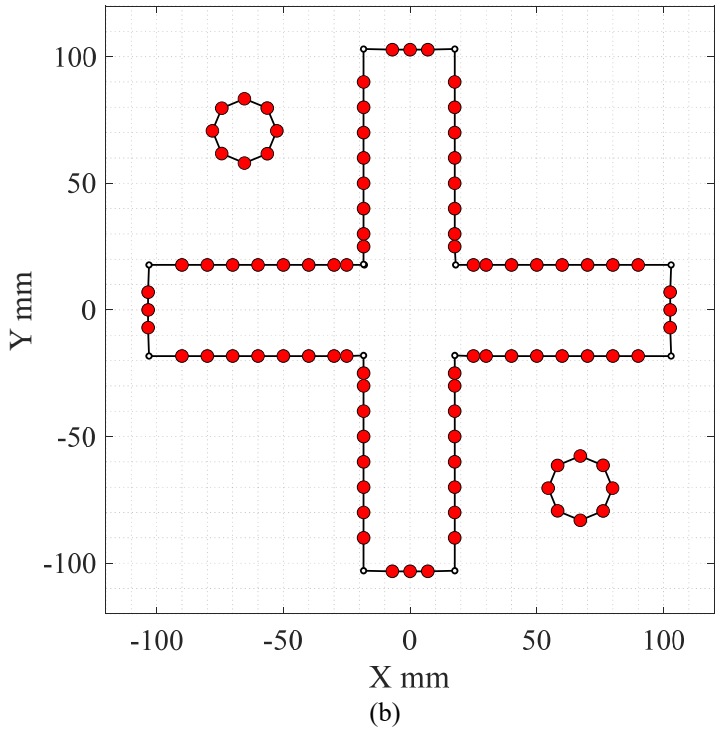

(b)

Figure 8 (a) Test setup with two precision spheres. (b) Target positions (red circles) to be measured on the workpiece surface, including two precision spheres.

4.3 Identification results

- Identified workpiece geometric errors

Figure 9(a) shows the "raw" probed profile measured at $C_1 = 0°$ (in blue circles), $\Delta\tilde{q}_{i,1}$ $(i = 1, 2, \ldots, N_w)$. For each nominal point ${}^{w}p_i^*$, shown in gray circles, the measured point is shown in the direction normal to the surface. The probed error, $\Delta\tilde{q}_{i,1}$, is magnified 2,500 times (as shown in "Error scale", 50 mm in Fig. 9(a) corresponds to an error of 20 μm).

Similarly, Fig. 9(b) compares all the "raw" geometric profiles measured at $C = 0°, 75°, 130°$, and $210°$, shown in the WCS. The measured geometric profiles differ at each C angle, owing to the influence of linear and rotary axis kinematic errors. If there is no kinematic error, each plot would be the same. The linear offset is largely attributable to the offset of the workpiece position from the C-axis of rotation, but the influence of linear axis error motions is also observable from the difference in the measured profiles.

For the comparison, the "true" geometry was measured at the same points by using a CMM (PMM-C700P by Brown & Sharpe (Leitz)). Its measurement uncertainty is $E = (0.6 + L/600)$ μm, where L denotes the measured length. The measured points by the CMM are shown in green diamonds in Fig. 9(a). Compared to the "true" geometry measured by the CMM, the probed profile at $C_1 = 0°$ shows an error of approximately 5 μm at maximum. This is caused by the machine tool's positioning error. It can be observed that the error is largely attributable to the squareness error of Y- to X-axis.

The workpiece geometric profile, $G_{\mathrm{normal}}({}^{w}p_i^*)$, identified by applying the present self-calibration algorithm, is shown in orange diamonds in Fig. 9(c). Compared with the "raw" probed trajectory in Fig. 9(a), measured at $C_j = 0°$, Fig. 9(c) shows that the self-calibration scheme significantly reduced the measurement error due to X- and Y-axis kinematic errors, resulting in the identified workpiece profile significantly closer to the "true" geometry.

In Fig. 9(c), near the nominal point ${}^{w}p_i^* = (80, 20)$ mm, a larger error is observed in the identified workpiece geometric profile (orange diamonds). The trajectory looks "looped" because the error is magnified to the direction normal to the surface at each point [37]. Similar error is observed in all the "raw" profiles in Fig. 9(b). However, the profile measured by the CMM in Fig. 9(c) does not contain this error. We consider that this may be caused by a chip or a dust on the probed workpiece surface, due to insufficient cleaning before the probing. This part should be ignored in the comparison with the CMM profile.

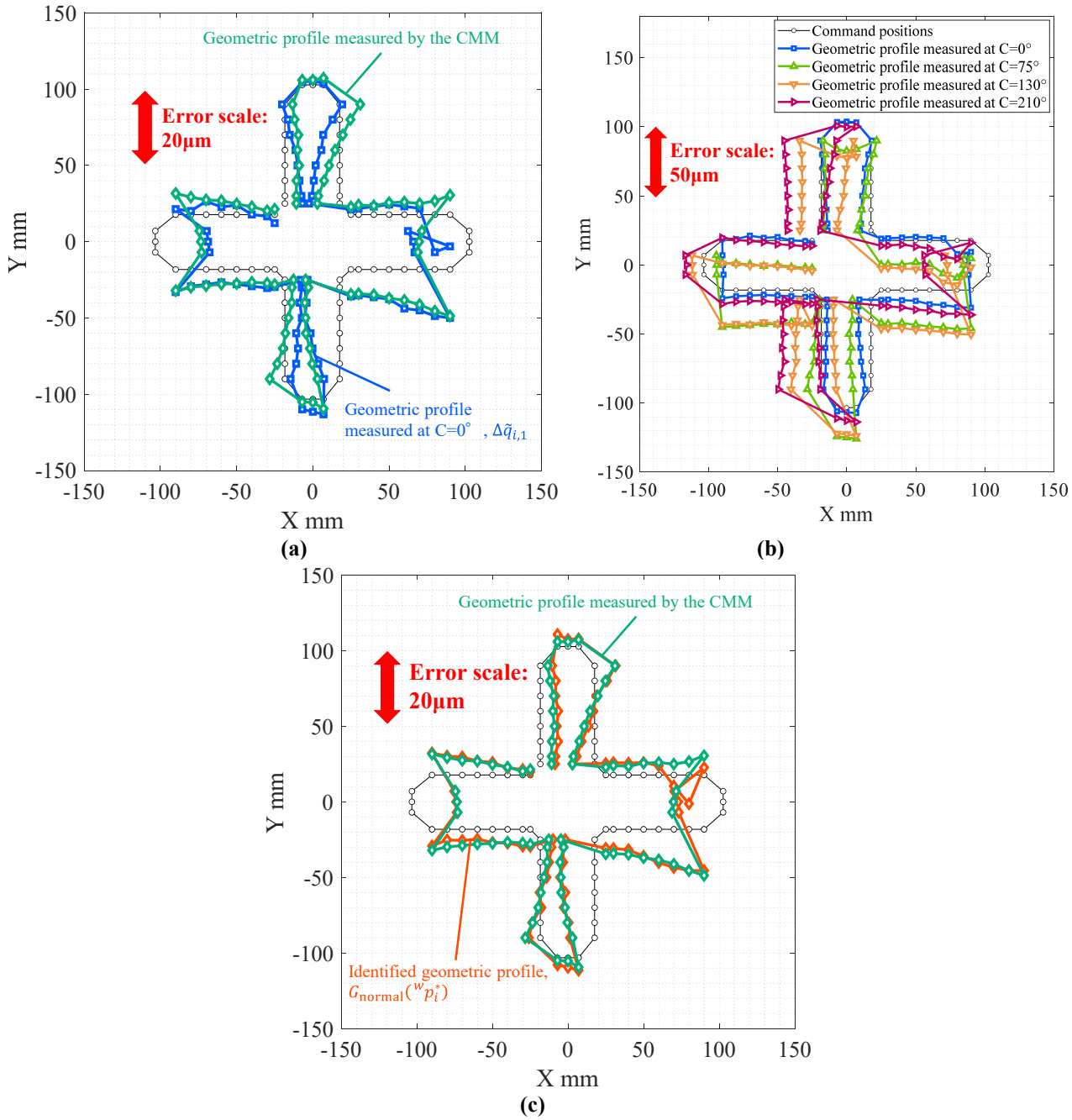

Figure 9 Comparison of the workpiece geometric profiles (a) measured at C=0° (blue circles) and measured by the CMM (green diamonds), (b)measured at C=0°, 75°, 130°, and 210°, (c) identified by the proposed scheme, $\boldsymbol{G_{\text{normal}}({}^{w}\boldsymbol{p}_i^*)}$ (orange diamonds) and measured by the CMM (green diamonds). The errors from the nominal positions (gray circles) are magnified 2,500 times in (a) and (c), 1,000 times in (b) (see "Error Scale"). The proposed algorithm was applied with all the probed points shown in Fig. 8(b), including those on the spheres.

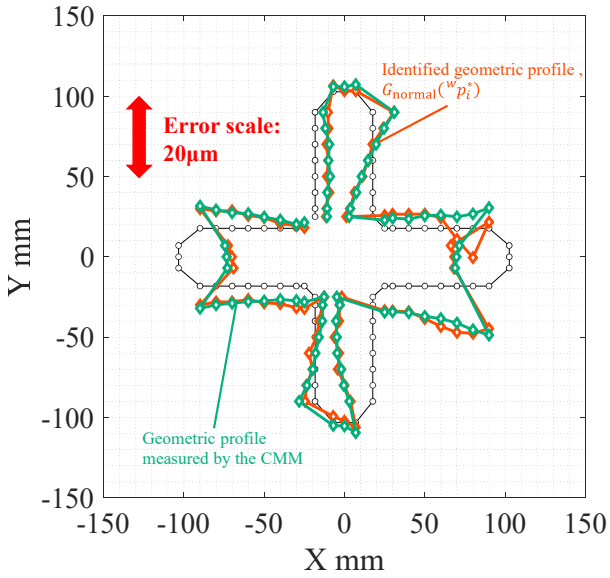

Figure 10 Comparison of the workpiece geometric profiles identified by the proposed scheme, $\boldsymbol{G_{\mathrm{normal}}({}^{w}p_i^*)}$ (orange plots) and measured by the CMM (green diamonds). The proposed algorithm was applied without the probed points on the spheres shown in Fig. 8(b).

To investigate the influence of the additional spheres, the proposed algorithm was applied without the probed points on the spheres shown in Fig. 8(b). Figure 10 (orange diamonds) shows the identified workpiece geometric profile, $G_{\mathrm{normal}}({}^{w}p_i^*)$, in comparison with the CMM measurement (green diamonds). Note that the orientation of the identified geometric profile in Fig. 10 was best-fit to the CMM profile for the comparison. In Fig. 9(c) and 10, the difference in the estimated workpiece geometric profiles with and without the spheres was not significant. According to the uncertainty analysis in Section 6 (Fig. 18(c) and 19), the uncertainty in the estimated workpiece geometric profile differs approximately by 4 μm between the two setups. This did not influence significantly in the experiment.

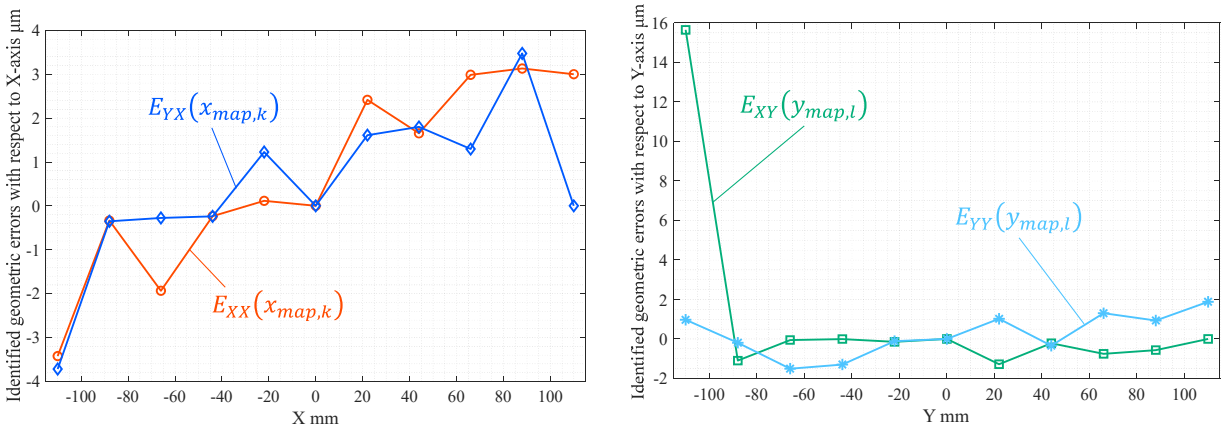

(a) (b)

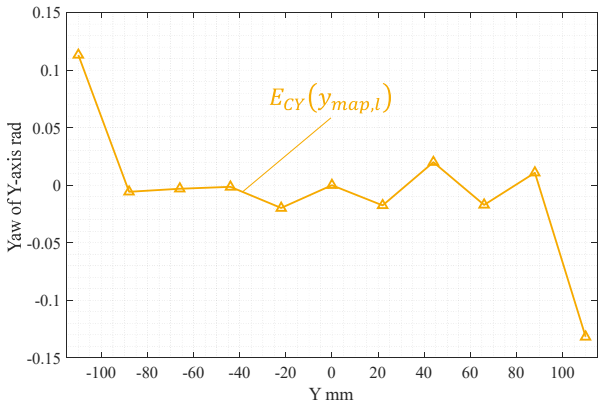

(c)

Figure 11 Geometric errors identified by the proposed algorithm, (a) $\boldsymbol{E_{XX}(x_{map,k})}$ and $\boldsymbol{E_{YX}(x_{map,k})}$, (b) $\boldsymbol{E_{YY}(y_{map,l})}$ and $\boldsymbol{E_{XY}(y_{map,l})}$, (c) $\boldsymbol{E_{CY}(y_{map,l})}$.

- Identified kinematic errors of X- and Y-axes

Figure 11 shows (a) $E_{XX}(x_{map,k})$ and $E_{YX}(x_{map,k})$, (b) $E_{YY}(y_{map,l})$ and $E_{XY}(y_{map,l})$, (c) $E_{CY}(y_{map,l})$, identified by the proposed algorithm (see Table 1 for their definitions). The identified squareness error between X- and Y-axis, $E_{C(0X)Y}$, was -43.4 μrad. All the probed points in Fig. 8(b) are taken into account, including those on the spheres. For comparison, the 2D positioning error by X- and Y-axes was directly measured by using a 2D digital scale, KGM181 by Heidenhain. In Figs. 12(a) and (b), the orange dashed-line grid points represent the command positions. At every grid point, the 2D positioning error was measured. The orange circles show the measured positions. The positioning errors from the command positions are magnified 1,000 times. In the measured range X120×Y180 mm, the positioning error was not significant; the maximum error was about 9 μm. However, the squareness error of Y- to X-axis, about 5 μm/180mm, can be clearly observed. Note that the measured range was smaller than the grid of $(x_{map,k}, y_{map,l})$ (dashed-line blue grid) due to the limited size of the scale grid of KGM181.

In Fig. 12(a), the blue grid points represent the estimated 2D positioning errors, $\left(E_{X,\text{total}}(x_{map,k}, y_{map,l}), E_{Y,\text{total}}(x_{map,k}, y_{map,l})\right)$, calculated by Eqs. (4) and (5) with the identified X- and Y-axis error motions. The blue dashed-line grid in Fig. 12 indicates the nominal positions, $(x_{map,k}, y_{map,l})$. Within the measurable range of the 2D digital scale (orange grid), the vertical lines in the blue grid in Fig. 12(a) are slightly tilted in clockwise direction, which indicates the squareness error of Y- to X-axis. Within this range, the estimated positioning errors match well with the cross grid encoder measurement. However, the orientation error of the topmost and bottommost lines of the estimated grid (blue grid) is clearly much larger than that of the cross grid encoder measurement (orange grid).

In Fig. 11 (b), the identified $E_{XY}(y_{map,l})$ is significantly larger at $y_{\text{map,l}}$ = -110 mm. Similarly, in Fig. 11 (c), the identified $E_{CY}(y_{map,l})$ is significantly larger at $y_{\text{map,l}}$ = -110 mm and +110 mm. These cause a larger orientation error on the topmost and bottommost lines of the estimated grid (blue grid) in Fig, 12(a). These are attributable to the uncertainty in identified geometric errors discussed in Section 6.2. Figure 20(a) in Section 6.2 shows a larger uncertainty at $y_{\text{map,l}}$ = -110 mm and +110 mm.

Figure 12(b) (blue grid) shows the 2D positioning errors, identified without the two spheres (the same setup as the one for Fig. 10). Compared to the setup with the spheres (Fig. 12(a)), the absence of the two spheres gave a significant impact on the estimated linear axis error motions, which matches well with the prediction by the uncertainty analysis in Section 6 (Figs. 20 (a) and (b)). But this did not disturb much the estimation of the workpiece geometry, as discussed above.

- Error motions of C-axis

Figure 13 shows the radial error motion of C-axis, $E_{XC,\text{total}}(C_j)$ and $E_{YC,\text{total}}(C_j)$, identified by the proposed scheme. If there is no error, $\left(E_{XC,\text{total}}(C_j), E_{YC,\text{total}}(C_j)\right)$ is at the origin for any C_j. The center of the best-fit circle to the trajectory in Fig. 13 represents the position error of the C-axis average line, (E_{X0C}, E_{Y0C}). Figure 13 gives that $(E_{X0C}, E_{Y0C}) = (15, 6)$ μm. Figure 14 shows the estimated angular positioning deviation of C-axis, $E_{CC}(C_j)$.

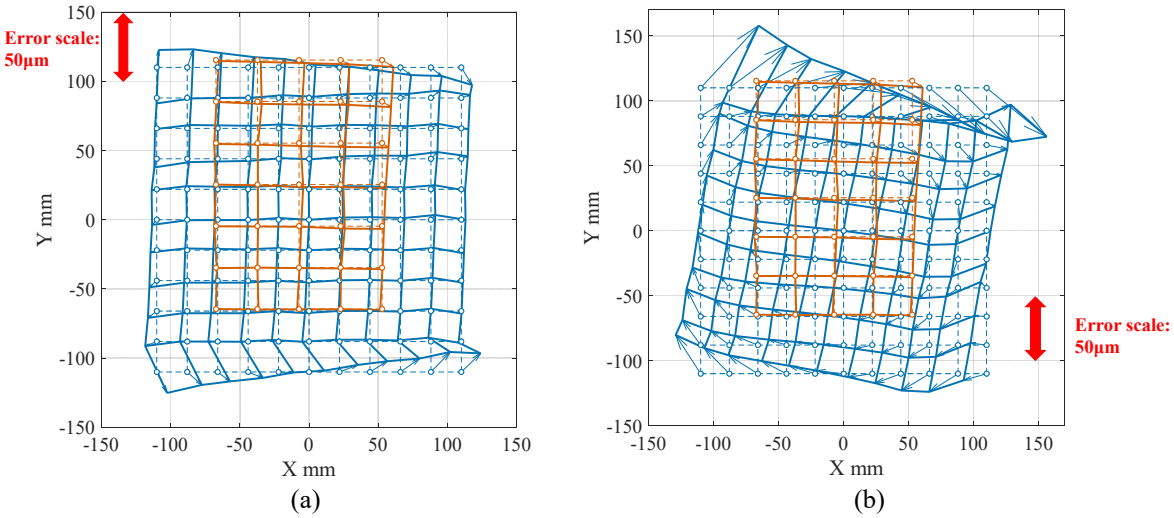

Figure 12 The error map measured by a 2D digital scale (orange grid) and the estimated error map constructed by the identified linear axes geometric errors (blue grid), (a) with precision spheres, (b)without precision spheres. The errors are magnified 1,000 times.

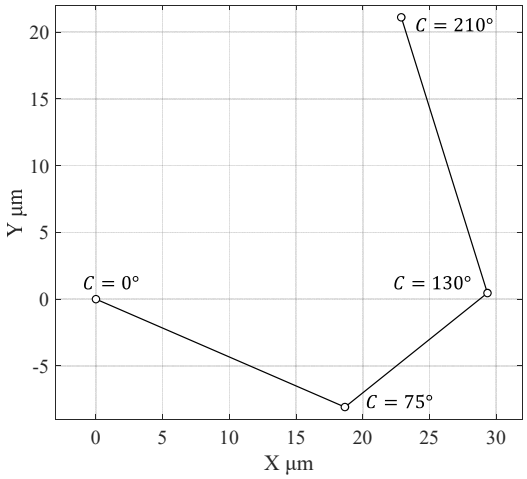

Figure 13 The trajectory of the C-axis centerline, $\boldsymbol{E_{XC,\mathrm{total}}(C_j)}$ and $\boldsymbol{E_{YC,\mathrm{total}}(C_j)}$, identified with precision spheres.

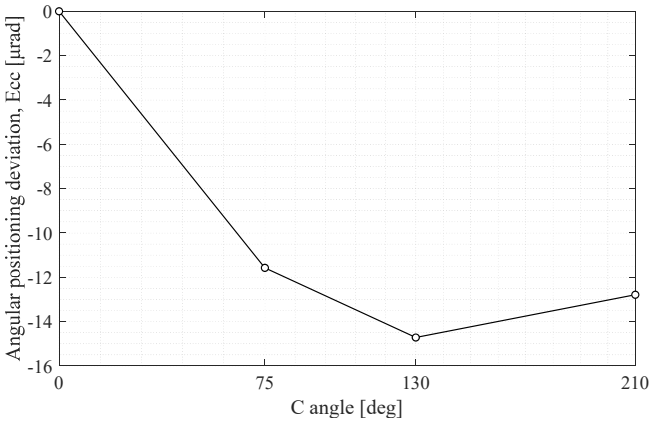

Figure 14 Angular positioning deviation of C-axis, $\boldsymbol{E_{CC}(C_j)}$, identified with precision spheres.

5. Case study #2: Application of the proposed self-calibration scheme to pin positions

5.1 Test objective and setup

An objective of the second case study is to apply the proposed scheme to a practical, industrial part. It is a frame part for an aircraft engine, manufactured in Kawasaki Heavy Industries, Ltd. The test piece in Case Study #1 contains nominally straight surfaces only, and thus some error motions, such as the linear positioning and angular (yaw) error motions of X- and Y-axes, have smaller influence on the finished workpiece geometry. The test piece in Case Study #2 contains holes, whose XY positions are to be measured. A larger class of X- and Y-axis error motions can influence the hole positions.

Figure 15 shows the geometry of the test piece (material: cast iron). The test objective is to measure the 2D position of the centerline of total 18 cylindrical pins, inserted to threaded holes located on a pitch circle of the nominal diameter 400 mm with nominal angular interval 20°. Note that the exact geometry of the test piece, as well as its photograph, cannot be disclosed due to the part customer's request. However, the pin locations to be probed are exact in Fig. 15.

The configuration of the machine tool is shown in Fig. 16. According to ISO 10791-2 [38], the kinematic chain of the machine tool is represented by: V[w-C-A-b-Y-X-Z-(C)-t]. Since X-axis is on the Y-axis, the same kinematic model in Eqs. (4) and (5) is applicable. A touch-trigger probe, RMP600 by Renishaw (the measurement uncertainty: 1.8 μm (k=2)), was used. The diameter of the stylus sphere was 6 mm.

Each cylindrical pin has the nominal diameter 12 mm, and its roundness and surface roughness are sufficiently small. On each pin, four points are probed at the same Z position to measure its centerline position. Similarly as in Case study #1, two additional spheres (material: ceramics, diameter: 30 mm) are put at the locations shown in Fig. 15. On each sphere, eight points are probed. Total 84 points are probed at every C angular position. In this experiment, this set was measured at:

$$C = 0°, 31°, 83°, 137°, 191°, 227°, 257°, 313° \tag{20}$$

These C angles were designed based on the uncertainty analysis presented in Section 6. The grid, where X- and Y-axis error motions are defined (see Fig. 6), was set at $x_{map,k} = -400, -320, -240, \ldots, +400$ mm and $y_{map,l} = -400, -320, -240, \ldots, +400$ mm (11 × 11 grid).

For comparison, the pin positions were measured by using a CMM.

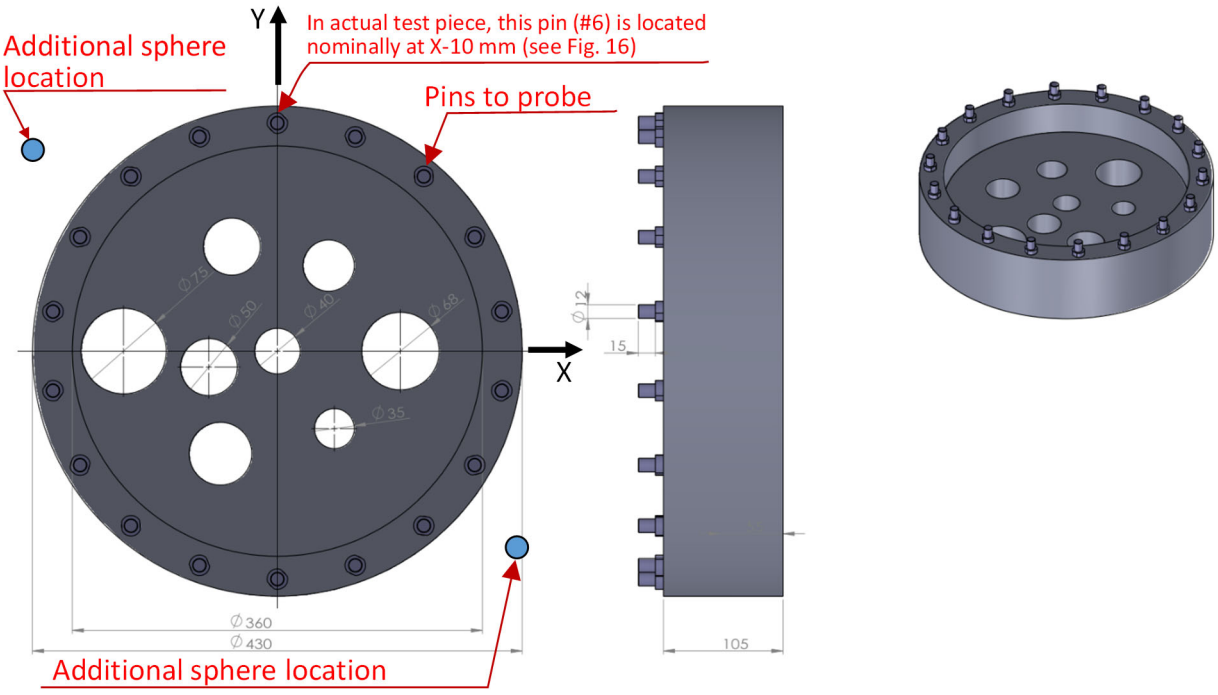

Figure 15 Test piece in Case Study #2. The 2D position of total 18 cylindrical pins, inserted to threaded holes located on a pitch circle of the nominal diameter 400 mm with nominal angular interval 20°, is probed. Actual location of pin #6 (see Fig. 17) is different from this diagram by X-10 mm.

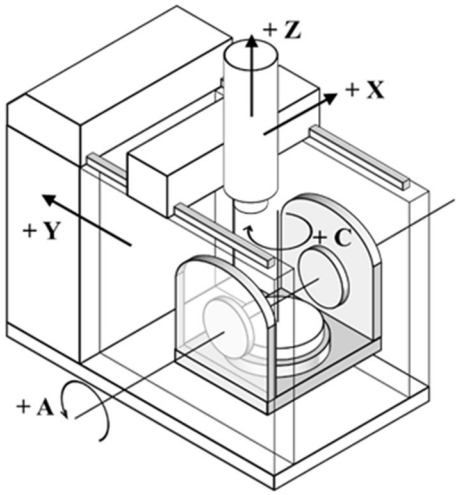

Figure 16 Configuration of the machine tool used in Case study #2

5.2 Identified pin positions

Figure 17 compares the pin positions measured by the CMM (black circles), the "raw" positions probed at C=0° (blue circles), and the ones identified by the proposed self-calibration (red circles). An error from the measured positions by the CMM is magnified 2,500 times, i.e. an error of 40 μm is shown as 100 mm, as indicated by "Error scale." In this measurement CS, the error is defined zero at the first pin. The direction of the X-axis is defined such that the 11th pin has no error in the Y-direction.

The "raw" pin positions probed at C=0° (blue circles) shows a measurement error of approximately 8 μm at maximum with the 13th pin. The linear positioning error of X-axis clearly influences the probed pin positions. Furthermore, the trajectory of probed positions looks slightly elliptical with its major axis tilted by 45° from the Y-axis, which is caused by the squareness error of Y- to X-axis.

The pin positions estimated by the proposed scheme (red circles) are significantly closer to the CMM measurement (black circles). The maximum error is within 2 μm.

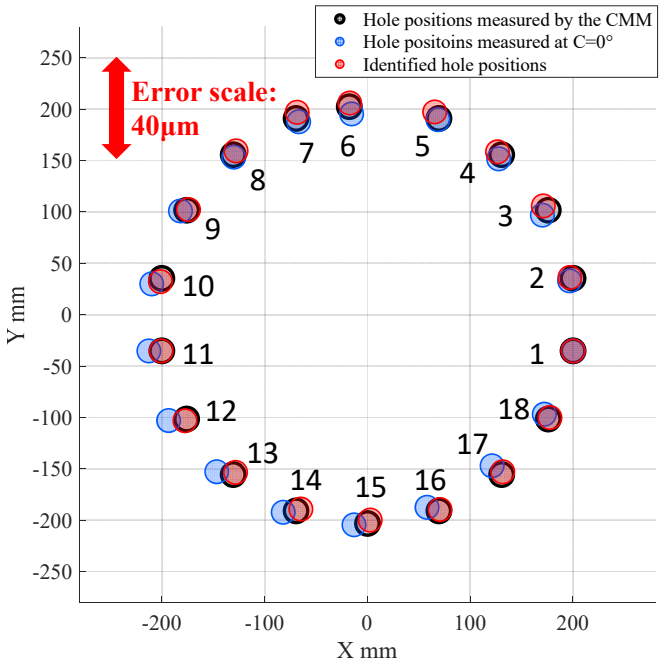

Figure 17 Comparison of the pin positions measured by the CMM (black circles), the ones probed at C=0° (blue circles) and the ones identified by proposed self-calibration scheme (red circles). Errors from the positions measured by the CMM are magnified 2,500 times.

6. Uncertainty analysis

In Fig. 12, it was experimentally shown that the uncertainty in the estimated error motions of linear axes can significantly change by adding spheres to probe. This indicates that the uncertainty in the proposed self-calibration scheme can heavily depend on the nominal geometry of the workpiece. It is thus essential to numerically assess the uncertainty to foresee if the present scheme can effectively reduce the uncertainty for the given nominal workpiece geometry. As the uncertainty contributor, this paper assessed the probing uncertainty, which is attributable to the probe itself and the machine tool's positioning repeatability. By the experiment shown in [23], the standard uncertainty (k=1) of the touch-trigger probing on this machining center was assessed 1.38 μm. To assess its propagation to the uncertainty in the estimates by the proposed scheme, Monte Carlo simulation with 1,000 run was applied to the algorithm proposed in Section 3.3. Analogous uncertainty assessment was presented for the roundness self-calibration in our previous work [24]. The uncertainty analysis is presented only for Case study #1.

6.1 Uncertainty in the identified workpiece geometry

- Influence of the number of C-axis angular positions

Figure 18 shows the assessed uncertainty (k=2) in the identified geometric error of the workpiece, $G_{\mathrm{normal}}({}^{w}p_i^*)$, with additional sphere measurement, when C-axis is indexed at 0° and 75° (Fig. 18(a)), at 0°, 75° and 130° (Fig. 18(b)), at 0°, 75°, 130° and 210° (Fig. 18(c)). To study the influence of the number of C-axis angles on the uncertainty, the three cases are compared. The expanded uncertainty (k=2) is shown by color. The maximum uncertainty is approximately 6.5 μm in Fig. 18(a), 3.0 μm in Fig. 18(b), and 2.1 μm in Fig. 18(c), respectively. Increasing the number of C angles leads to smaller uncertainty in the identified workpiece geometry.

- Influence of the additional spheres

Then, the influence of the additional spheres (see Fig. 8) on the uncertainty is studied. Figure 19 show the uncertainty of the identified geometric error of the workpiece, $G_{\mathrm{normal}}({}^{w}p_i^*)$, without sphere measurement when C-axis is indexed at 0°, 75°, 130° and 210°. Compared to Fig. 18(c), Fig. 19 shows larger uncertainty, but the difference is not significant. The maximum difference is approximately 4 μm, and larger difference is only near the edges of the grooves.

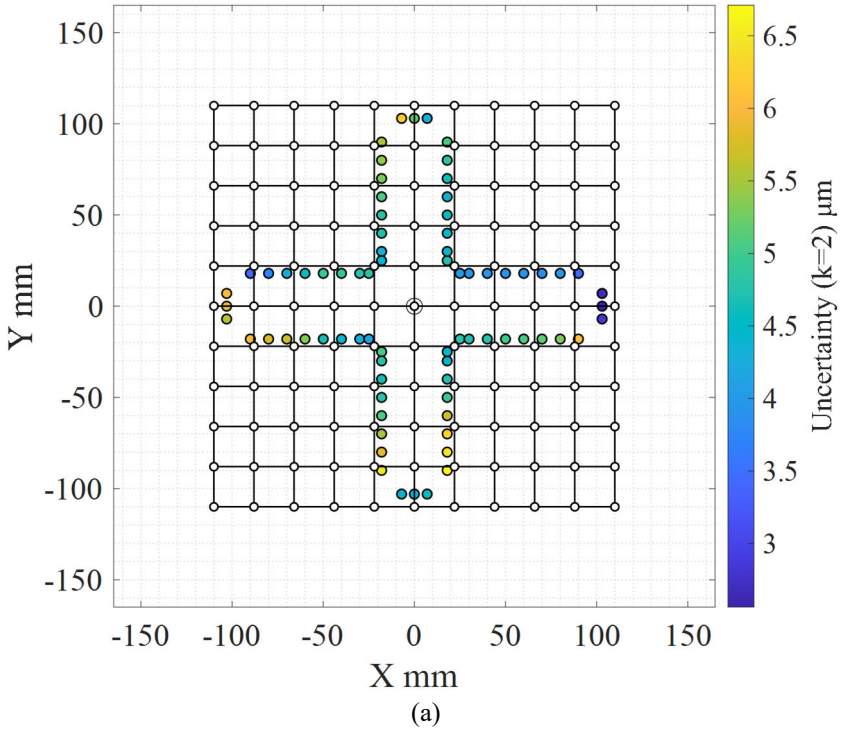

(a)

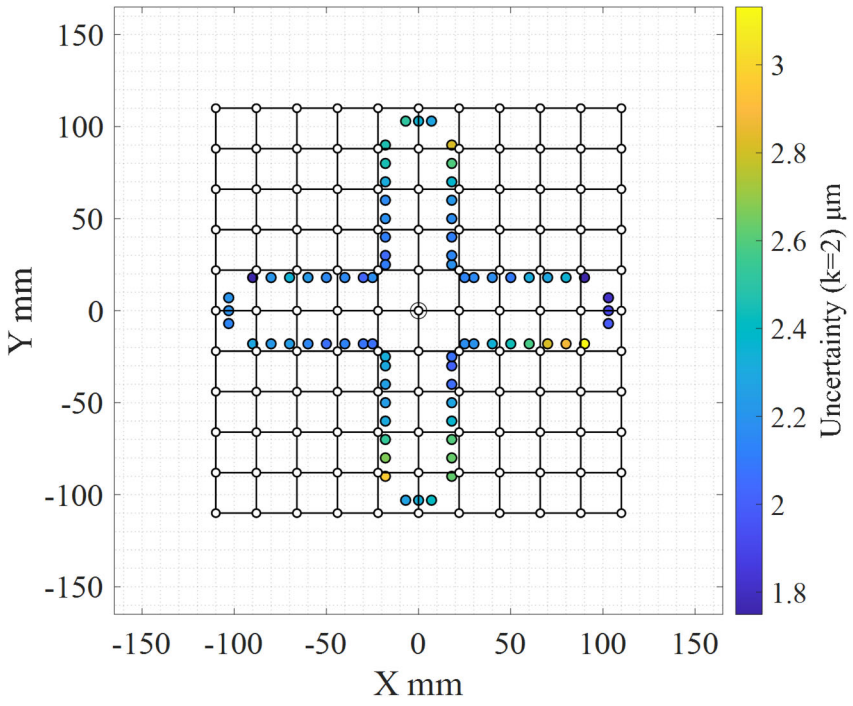

(b)

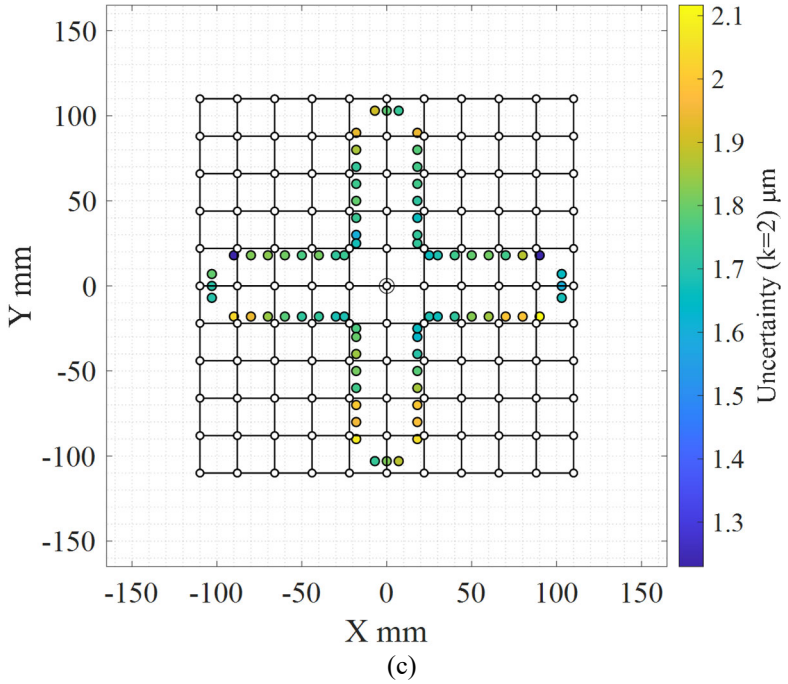

(c)

Figure 18 Uncertainty (k=2) in the identified workpiece geometric error profile with the additional sphere measurement, as (a) C-axis is indexed at 0 and 75°, (b) C-axis is indexed at 0°, 75° and 130°, (c) C-axis is indexed at 0°, 75°, 130° and 210°.

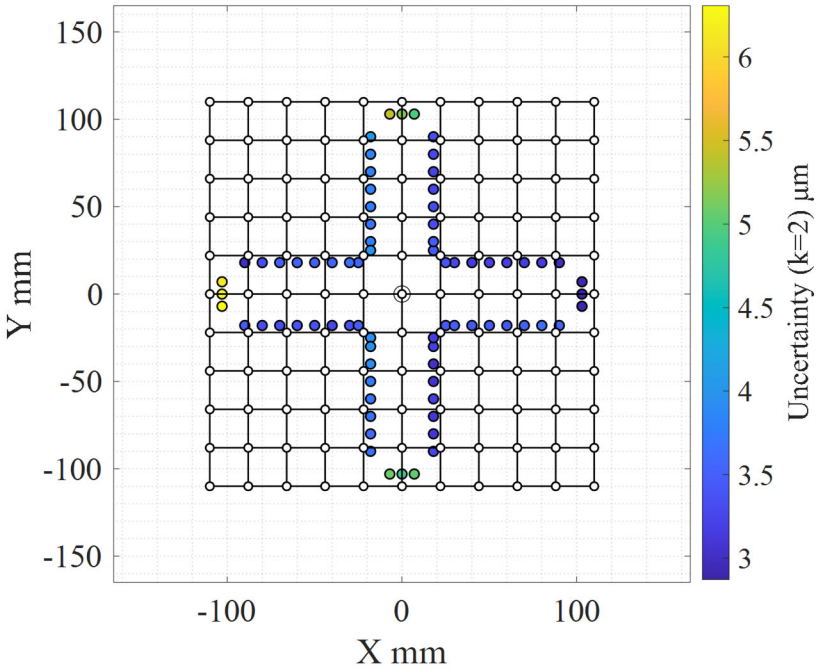

Figure 19 Uncertainty (k=2) in the identified workpiece geometric error profile, without additional sphere measurement. C-axis is indexed at 0°, 75°, 130° and 210°.

6.2 Uncertainty in the identified linear and rotary axis error motions

Figure 20 shows the assessed uncertainty (k=2) in the 2D positioning errors constructed by the identified linear axis kinematic errors by Eqs. (4) and (5). The uncertainty at (0,0) is 0 because of Eq. (16). In a large portion of the workspace, the uncertainty was smaller than 10 µm. At Y=110 and -110 mm, however, it was remarkably larger, 28 µm at maximum in Fig. 20 (a). This is mainly caused by the uncertainty in the identified yaw of Y-axis, $E_{CY}(110)$ and $E_{CY}(-110)$. Error motions at Y=110 and -110 mm affect fewer probed points. As a result, the uncertainty in the probed positions is propagated to larger uncertainty in the estimated error motion at Y=110 and -110 mm.

In the experiment, when no additional sphere was probed, Fig. 12(b) shows significantly larger positioning error at Y=-110 and 110 mm, which is largely due to the estimation error. This corresponds well with the uncertainty assessment shown in Fig. 20(b).

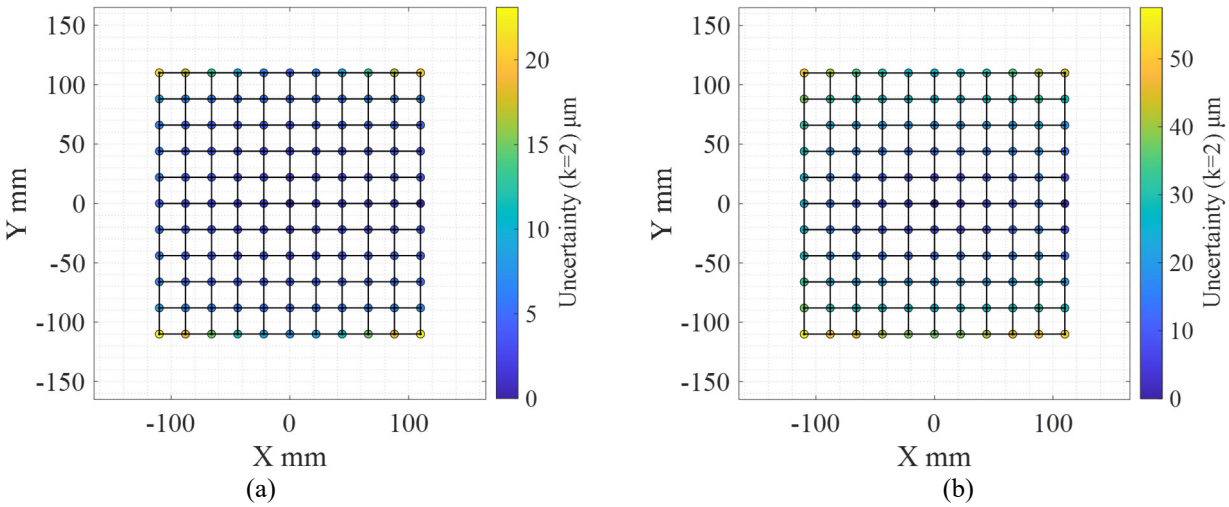

Figure 20 Uncertainty (k=2) in the 2D positioning errors constructed by the identified X- and Y-axis kinematic errors, when C-axis is indexed at 0°, 75°, 130° and 210°, (a) with two spheres, (b) with no sphere.

Table 2 Uncertainty (k=2) in the identified C-axis error motions with the sphere measurement

C angle [deg]	$U_{XC,\mathrm{total}}$[μm]	$U_{YC,\mathrm{total}}$[μm]	U_{CC}[μrad]
0	0.0	0.0	0.0
75	1.0	0.9	8.9
130	1.2	1.1	9.3
210	1.2	1.2	8.2

Table 2 summarized the uncertainty (k=2) of the identified C-axis error motions with the spheres measured. $U_{\mathrm{XC,total}}$, $U_{\mathrm{YC,total}}$ and U_{CC} represent the uncertainty in the radial error motion, $E_{XC,\mathrm{total}}(C_j)$, $E_{YC,\mathrm{total}}(C_j)$, and the angular positioning error motion, $E_{CC}(C_j)$, respectively. Considering the angular positioning resolution of C-axis (0.001°=17 μrad), U_{CC} seems to be sufficiently small.

It must be emphasized that the main objective of the proposed scheme is to estimate the geometry of the workpiece. Figure 20 shows that the uncertainty in the estimated error motions of X- and Y-axes is larger at Y = -110 mm and +110 mm. It indicates that that it may be difficult to accurately estimate the error motions at Y = -110 mm and +110 mm by the proposed scheme. However, the uncertainty in the identified workpiece geometry, shown in Fig. 18(c), is significantly smaller than that in the linear axis error motions, shown in Fig. 20(a). These uncertainty assessments comply with the experimental results. In the experiment, the identified linear axis positioning errors show larger estimation error near the edge of the workspace, as can be observed in Fig. 12(a). However, it does not significantly increase the estimation error in the workpiece geometry, as is experimentally validated in Fig. 9(c).

7. Conclusion

This study proposed a self-calibration scheme for on-machine 2D geometric measurement. On the assumption that the 2D positioning error of linear axes is given by the rigid-body kinematic model, the proposed scheme can identify the geometric profile of the workpiece with eliminating the influence of linear axis geometric errors.

The cross-shaped pocket test piece, in the first case study in Section 4, is nominally symmetric with respect to the origin. Therefore, as illustrated in Fig. 1, the conventional self-calibration scheme may be, in principle, applicable, when the test piece is rotated by a multiple of 90°. The unique contribution of the proposed self-calibration scheme could be further illustrated when it is applied to a point-asymmetric test piece. Such an application will be further studied in our future research.

In the proposed scheme, the uncertainty in the estimated workpiece geometry can heavily depends on its nominal geometry, in other words, the distribution of the probed points. According to the uncertainty assessment in Section 6, in the experiment, extra probed points were added by adding two spheres to probe. The experiment showed they significantly reduced an estimation error of linear axis error motions particularly near the edges of the workspace.

Such an uncertainty analysis helps a user to intuitively understand for what workpiece geometry the proposed self-calibration scheme is more effective. For example, for a nominally circular disk, placed concentric to the C-axis, all the probed points would be nominally on a single circle, even when the C-axis is indexed at various angles. As a result, it can be predicted that the error motions at some grid points (see Fig. 6) may not be identifiable, or their uncertainty can be unacceptably large. Furthermore, clearly, the probing on a nominally circular surface is completely insensitive to the angular positioning error of C-axis. These observations indicate that the proposed scheme cannot identify all the error motions of X-. Y- and C-axes, when applied to a nominally circular disk. However, this does not mean it cannot identify the geometry of a nominally circular disk. The self-calibration for the roundness measurement is well established. The uncertainty assessment, as presented in Section 6, is essential to foresee how effective the proposed scheme is for the given workpiece nominal geometry.

The proposed scheme requires longer measurement time. Given that environmental conditions on a shop floor can change continuously, it is preferable that the proposed scheme should be conducted in a short time. Otherwise, the change in machine tool's error motions during the measurement can be a major uncertainty contributor for the proposed scheme.

Acknowledgements

We would like to express our appreciation to Mr. Keiji Maeta, in Hiroshima Prefectural Technology Research Institute, West Region Industrial Research Center, Hiroshima, Japan, for his support with the CMM measurement.

Declaration of competing interest

The authors declare that they have no known competing financial interests or personal relationships that could have appeared to influence the work reported in this paper.

References

[1] U. Mutilba, E. Gomez-Acedo, G. Kortaberria, A. Olarra, J.A. Yagüe-Fabra, Traceability on machine tool metrology: a review, Sensors. 17(7) (2017) 1605.
[2] K. Simson, l. Lillepea, B. Hemming, T. Widmaier, “Traceable in-process dimensional measurement - European Metrology Research Programme, project No. IND62”, Proc. 9th International DAAAM Baltic Conference INDUSTRIAL ENGINEERING, Apr. 2014.
[3] ISO/PWD TR 230-13:2022, Test code for machine tools — Part 13: Guidelines for the determination of the measuring performance of machine tools used as coordinate measuring machines
[4] ISO 15530-3, Geometrical product specifications (GPS) — Coordinate measuring machines (CMM): Technique for determining the uncertainty of measurement — Part 3: Use of calibrated workpieces or measurement standards, 2011.
[5] ISO/TS 15530-4, Geometrical Product Specifications (GPS) — Coordinate measuring machines (CMM): Technique for determining the uncertainty of measurement — Part 4: Evaluating task-specific measurement uncertainty using simulation, 2008.
[6] Verein Deutscher Ingenieure (VDI), VDI/VDE 2617-11-accuracy of coordinate measuring machines - characteristics and their checking - determination of the uncertainty of measurement for coordinate measuring machines using uncertainty budgets, 2011.
[7] R. Klobucar, B. Acko, Experimental evaluation of ball bar standard thermal properties by simulating real shop floor conditions, Int. J. Simulat. Modell. 15 (3) (2016) 511–521.
[8] F. Viprey, H. Nouira, S. Lavernhe, C. Tournier, Novel multi-feature bar design for machine tools geometric errors identification, Precs. Eng. 46 (2016) 323–338.
[9] J. Sładek, A. Gąska, Evaluation of coordinate measurement uncertainty with use of virtual machine model based on Monte Carlo method, Measurement 45 (2012) 1564–1575.
[10] Y. Miura, S. Nakanishi, E. Higuchi, et al., Comparative evaluation of estimation of hole plate measurement via Monte Carlo simulation, Precis. Eng. 56 (2019) 496–505.
[11] ISO 10360-2, Geometrical Product Specifications (GPS) – Acceptance and reverification tests for coordinate measuring machines (CMM) — Part 2: CMMs used for measuring linear dimensions, 2009.
[12] ISO 10360-5, Geometrical Product Specifications (GPS) – Acceptance and reverification tests for coordinate measuring machines (CMM) — Part 5: Coordinate measuring machines (CMMs) using single and multiple stylus contacting probing systems using discrete point and/or scanning measuring mode, 2020.
[13] H. Schwenke, W. Knapp, H. Haitjema, et al., Geometric error measurement and compensation of machines–an update, CIRP Annals. 57 (2) (2008) 660–675.
[14] S. Ibaraki, W. Knapp, Indirect measurement of volumetric accuracy for three-axis and five-axis machine tools: a review, Int. J. Autom. Technol. 6 (2) (2012) 110–124.
[15] W. Gao, S. Ibaraki, M. A. Donmez, D. Kono, J. R. R. Mayer, Y.-L. Chen, K. Szipka, A. Archenti, J.-M. Linares, N. Suzuki, Machine tool calibration: Measurement, modeling, and compensation of machine tool errors, International Journal of Machine Tools and Manufacture, 187 (2023) 104017.
[16] B. Bringmann, A. Küng, W. Knapp, A measuring artefact for true 3D machine testing and calibration, CIRP Ann. Manuf. Technol. 54 (1) (2005) 471–474.
[17] A. Breitzke, H. Wolfgang, Workshop-suited geometric errors identification of three-axis machine tools using on-machine measurement for long term precision assurance, Precis. Eng. 75 (2022) 235–247.
[18] S. Ibaraki, T. Kudo, T. Yano, T. Takatsuji, S. Osawa, O. Sato, Estimation of Three-dimensional Volumetric Errors of Machining Centers by a Tracking Interferometer, Precision Engineering, 39 (2014) 179-186.
[19] J. Guillory, D. Truong, J.-P. Wallerand, Uncertainty assessment of a prototype of multilateration coordinate measurement system, Precis. Eng. 66 (2020) 496–506.
[20] K.I. Lee, S.H. Yang, Measurement and verification of position-independent geometric errors of a five-axis machine tool using a double ball-bar, Int. J. Mach. Tool Manufact. 70 (2013) 45–52.
[21] Z. Wang, D. Wang, S. Yu, et al., A reconfigurable mechanism model for error identification in the double ball bar tests of machine tools, Int. J. Mach. Tool Manufact. 165 (2021) 103737.
[22] C.V. Evans, RJ. Hocken, W.T. Estler, Self-calibration: Reversal, redundancy, error separation, and ‘absolute testing’, CIRP Ann. Manuf. Technol. 45 (2) (1996) 617–634.
[23] S. Onishi, S. Ibaraki, T. Kato, et al., A self-calibration scheme to monitor long-term changes in linear and rotary axis geometric errors, Measurement. 196 (15) (2022) 111183.
[24] N.Zimmermann, S. Ibaraki, Self-calibration of rotary axis and linear axes error motions by an automated on-machine probing test cycle, Int. J. Adv. Manuf. Technol. 107(5-6) (2020) 2107–2120.
[25] T. Watanabe, H. Fujimoto, Application of a self-calibratable rotary encoder, J. Physics: Conference Series, 13 (2005) 240–245.
[26] S. Huang, Precise Compensation for Positional Accuracy of Ultra-Precision Air-Bearing Motion Stage Based on the Self-Calibration Method, Int. J. Precis. Eng. Manuf. 22 (2021) 1039–1048.
[27] A. Guenther, D. Stöbener, G. Goch, Self-calibration method for a ball plate artefact on a CMM, CIRP Ann. Manuf. Technol. 65 (2016) 503–506.
[28] W. Gao, M. Tano, T. Araki, et al., Measurement and compensation of error motions of a diamond turning machine,

Precis. Eng. 31(3) (2007) 310–316.
[29] W. Gao, Precision Nanometrology: Sensors and Measuring Systems for Nanomanufacturing, Springer, (2010).
[30] H. Shimizu, R. Yamashita, T. Hashiguchi, et al., Square Layout Four-Point Method for Two-Dimensional Profile Measurement and Self-Calibration Method of Zero-Adjustment Error, Int. J. Autom. Technol. 12 (5) (2018) 707–713.
[31] N. Irino, M. Shimoike, K. Mori, et al., A vision-based machine accuracy measurement method, CIRP Ann. Manuf. Technol. 69(1) (2020) 445–448.
[32] J. Ye, M. Takac, C.N. Berglund, et al., An exact algorithm for self-calibration of two-dimensional precision metrology stages, Precis. Eng. 20(1) (1997) 16–32.
[33] Q.C. Dang, S. Yoo, S.-W. Kim, Complete 3-D self-calibration of coordinate measuring machines, CIRP Ann. Manuf. Technol. 55(1) (2006) 527–530.
[34] ISO 230-10:2022, Test code for machine tools — Part 10: Determination of the measuring performance of probing systems of numerically controlled machine tools.
[35] ISO 230-1:2012, Test code for machine tools — Part 1: Geometric accuracy of machines operating under no-load or quasi-static conditions.
[36] ISO 230-7:2015, Test code for machine tools — Part 7: Geometric accuracy of axes of rotation.
[37] S. Ibaraki, A. Matsubara, On the magnification of two-dimensional contouring errors by using contour-parallel offsets, Precision Engineering, 33(4) (2009) 322-326.
[38] ISO 10791-2:2023, Test conditions for machining centres — Part 2: Geometric tests for machines with vertical spindle (vertical Z-axis)